

Analysis of extreme ultraviolet spectra of laser-produced Cd plasmas

Mohammedelnazier Bakhiet, Maogen Su(苏茂根), Shiquan Cao(曹世权), Qi Min(敏琦), Duixiong Sun(孙对兄), Siqi He(何思奇), Lei Wu(吴磊), Chenzhong Dong(董晨钟)

Citation: Chin. Phys. B . 2020, 29(7): 075203 . **doi:** 10.1088/1674-1056/ab8894
Journal homepage: http://cpb.iphy.ac.cn; http://iopscience.iop.org/cpb

What follows is a list of articles you may be interested in

Analysis of extreme ultraviolet spectral profiles of laser-produced Cr plasmas

L Wu(吴磊), M G Su(苏茂根), Q Min(敏琦), S Q Cao(曹世权), S Q He(何思奇), D X Sun(孙对兄), C Z Dong(董晨钟)
Chin. Phys. B . 2019, 28(7): 075201 . **doi:** 10.1088/1674-1056/28/7/075201

Properties of long light filaments in natural environment

Shi-You Chen(陈式有), Hao Teng(滕浩), Xin Lu(鲁欣), Zong-Wei Shen(沈忠伟), Shuang Qin(秦爽), Wen-Shou Wei(魏文寿), Rong-Yi Chen(陈荣毅), Li-Ming Chen(陈黎明), Yu-Tong Li(李玉同), Zhi-Yi Wei(魏志义)
Chin. Phys. B . 2018, 27(8): 085203 . **doi:** 10.1088/1674-1056/27/8/085203

Laser-driven relativistic electron dynamics in a cylindrical plasma channel

Pan-Fei Geng(耿盼飞), Wen-Juan Lv(吕文娟), Xiao-Liang Li(李晓亮), Rong-An Tang(唐荣安), Ju-Kui Xue(薛具奎)
Chin. Phys. B . 2018, 27(3): 035201 . **doi:** 10.1088/1674-1056/27/3/035201

Dense pair plasma generation by two laser pulses colliding in a cylinder channel

Jian-Xun Liu(刘建勋), Yan-Yun Ma(马燕云), Tong-Pu Yu(余同普), Jun Zhao(赵军), Xiao-Hu Yang(杨晓虎), De-Bin Zou(邹德滨), Guo-Bo Zhang(张国博), Yuan Zhao(赵媛), Jing-Kang Yang(杨靖康), Han-Zhen Li(李汉臻), Hong-Bin Zhuo(卓红斌), Fu-Qiu Shao(邵福球), Shigeo Kawata
Chin. Phys. B . 2017, 26(3): 035202 . **doi:** 10.1088/1674-1056/26/3/035202

Detailed calibration of the PI-LCX: 1300 high performance single photon counting hard x-ray CCD camera

Wei Hong(洪伟), Xian-Lun Wen(温贤伦), Lai Wei(魏来), Bin Zhu(朱斌), Yu-Chi Wu(吴玉迟), Ke-Gong Dong(董克攻), Chun-Ye Jiao(焦春晔), Bo Wu(伍波), Ying-Ling He(何颖玲), Fa-Qiang Zhang(张发强), Wei-Min Zhou(周维民), Yu-Qiu Gu(谷渝秋)
Chin. Phys. B . 2017, 26(2): 025204 . **doi:** 10.1088/1674-1056/26/2/025204

Analysis of extreme ultraviolet spectra of laser-produced Cd plasmas*

Mohammedelnazier Bakhiet[1,3], Maogen Su(苏茂根)[1,2,†], Shiquan Cao(曹世权)[1], Qi Min(敏琦)[1], Duixiong Sun(孙对兄)[1], Siqi He(何思奇)[1], Lei Wu(吴磊)[1], and Chenzhong Dong(董晨钟)[1,2,‡]

[1] *Key Laboratory of Atomic and Molecular Physics & Functional Material of Gansu Province, College of Physics and Electronic Engineering, Northwest Normal University, Lanzhou* 730070, *China*

[2] *Joint Laboratory of Atomic and Molecular Physics, Northwest Normal University and Institute of Modern Physics of Chinese Academy of Sciences, Lanzhou* 730070, *China*

[3] *Department of Physics, Faculty of Education, University of the Holy Quran and Islamic Sciences, P. O. Box* 1459, *Khartoum* 14412, *Sudan*

(Received 25 February 2020; revised manuscript received 25 March 2020; accepted manuscript online 12 April 2020)

In order to provide detailed information about Cd structure and gain more insight regarding ionization degrees and types of transition, as well as the understanding of the temporal evolution behavior of laser produced Cd plasmas, extreme ultraviolet spectra of laser-produced cadmium (Cd) plasmas have been measured in the 8.4–12 nm region using spatio-temporally resolved laser-produced plasma spectroscopy technique. Spectral features were analyzed by the Hartree–Fock (HF) method with relativistic correlations (HFR) using the Cowan code. The results showed that the 4p–5s resonance transition arrays from Cd^{9+} to Cd^{13+} merged to form intense lines in this spectral region. A number of new spectral features from Cd^{9+} and Cd^{10+} ions are reported in this study. Based on the assumption of a normalized Boltzmann distribution among the excited states associated with a steady-state collisional–radiative model, the plasma parameters were obtained by comparing the experimental and simulated spectra. As a result, we succeeded in reproducing the synthetic spectra for different time delays, which yielded good agreement with the experiments. The temporal evolution behaviors of electron temperature and electron density of plasma were also analyzed.

Keywords: extreme ultraviolet spectra, laser-produced plasmas, collisional–radiative model, cadmium

PACS: 52.38.−r, 52.38.Mf, 52.50.−b, 52.50.Jm **DOI:** 10.1088/1674-1056/ab8894

1. Introduction

An accurate understanding of the evolution of laser-produced plasmas (LPPs) spectral structures would be very helpful to determine the radiation properties and hydrodynamic evolution of plasmas.[1,2] There are direct applications in many areas of important research, such as nuclear fusion,[3,4] astrophysics,[5] laboratory plasmas as ion sources,[6,7] and short wavelength light sources[8] for extreme ultraviolet (EUV) lithography.[9–11] Spectroscopic data concerning highly ionized fifth period atoms are important for work in tokamaks and some appear as impurities, such as zirconium and molybdenum.[12] In the last decades, several theoretical and experimental studies on the 4p–5s transition of various elements have been widely studied through their isoelectronic sequences.[13–17] In theoretical studies, the Hartree–Fock with configuration interaction (HFCI) method developed by Cowan[18] and some other computer programs are commonly performed.

Ryabtsev and Kononov[19] systematically observed the spectra of Rh^{7+}, Pd^{8+}, Ag^{9+}, and Cd^{10+} in 14–33 nm and about 100 lines in each spectrum from $4p^64d^2$–$(4d5p+4d4f+4p^54d^3)$ transitions were reported. Costello and O'Sullivan[20] observed and analysed the spectra from highly ionized Cd LPPs in the 8–11 nm range emitted by 4p–5s transitions from Cd^{11+} to Cd^{13+}; the spectra were produced by focusing a ruby laser (1.5 J, 25 ns) pulse onto pure Cd and $Cd(NO_3)_2$ targets. Their analysis was based on Hartree–Fock and Dirac–Fock with Froese–Fischer and Grant codes.[21,22] The analysis allowed the identification of a number of lines from 4p–5s transitions. However, a full description of the Cd spectrum in the 8–11.8 nm region remains unanalyzed to date.

This study analyzed the EUV spectra of Cd ions from LPPs. The overall objective was to provide detailed information about Cd structure and gain more insight regarding ionization degrees and types of transitions, as well as analyze the temporal evolution behavior. The 8.4–12 nm spectra produced from Cd ions are measured by using spatio-temporally resolved laser-produced plasma spectroscopy. Detailed atomic structure calculations were performed by the Hartree–Fok (HF) method with relativistic correlations (HFR) using the Cowan code. A number of new spectral features were identified from the experimental and calculated results. The collisional–radiative (CR) model[23] was able to deduce the charge distribution, plasma parameters, and ion fractions for different ion stages of Cd LPPs.

*Project supported by the National Key Research and Development Program of China (Grant No. 2017YFA0402300), the National Natural Science Foundation of China (Grant Nos. 11874051, 11904293, and 61965015), and the Special Fund Project for Guiding Scientific and Technological Innovation of Gansu Province, China (Grant No. 2019zx-10).

†Corresponding author. E-mail: nwnu_sumg@163.com

‡Corresponding author. E-mail: dongcz@nwnu.edu.cn

© 2020 Chinese Physical Society and IOP Publishing Ltd

2. Experiment

The experimental device is shown in Fig. 1. A detailed description of the experimental procedures has been previously reported.[24] Briefly, a tightly focused 1064 nm Nd:YAG laser with a 10 ns pulse width was used to produce plasmas from a planar metallic Cd target. The EUV radiation was coupled to a 10 μm-entrance slit of a focal-length 1.0 m-grazing-incidence spectrometer, equipped with 600 grooves/mm grating. Spectra were acquired with a 40 mm diameter microchannel plate detector coupled, via a coherent fiber optic bundle, to a 1024×255 pixel charge-coupled device (CCD). The microchannel gate width was 60 ns and the entrance slit width was 10 μm. The peak of the laser pulse on the target surface was defined as time zero for plasma production, as monitored by an oscilloscope.

The target holder was positioned on a three-dimensional translation stage (0.1 mm resolution) to provide a fresh surface for each laser shot and avoid forming deep craters. A lens positioned on a linear translation stage with the same resolution could be moved along the laser beam direction for convenient adjustment of laser focusing. Spectra were recorded 0.5 mm from the target surface. Known lines from the LPPs spectra of highly charged Al and Si ions were used to calibrate the spectrometer wavelength. Figure 2 shows the measured emission spectra of the laser-produced Cd plasmas after different time delays, measured at a laser power density of 2×10^{11} W/cm^2. Spectral intensity along the wavelength range varied with increasing time delay. Several intense narrow peaks were observed at 8.95 nm, 9.42 nm, 10.25, 10.66 nm, and 11.49 nm with widths of ∼0.05 nm, 0.03 nm, 0.02 nm, 0.03 nm, and 0.02 nm, respectively.

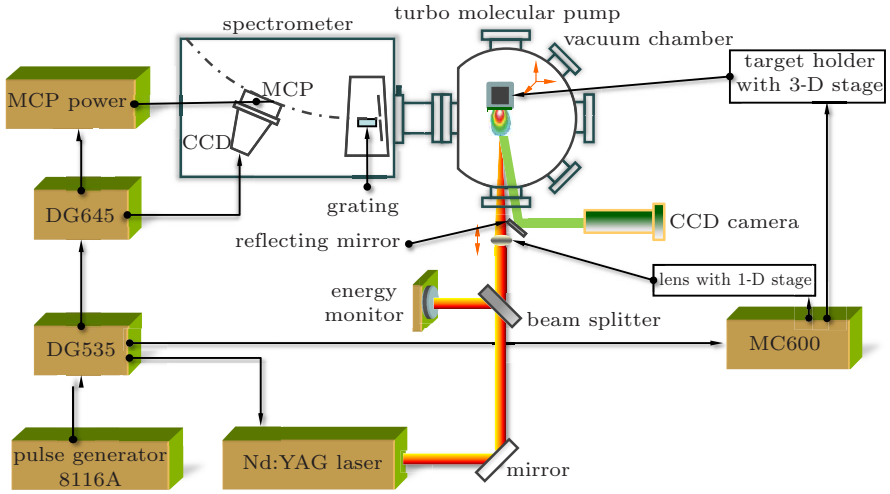


Fig. 1. Schematic of an LPP experimental setup.

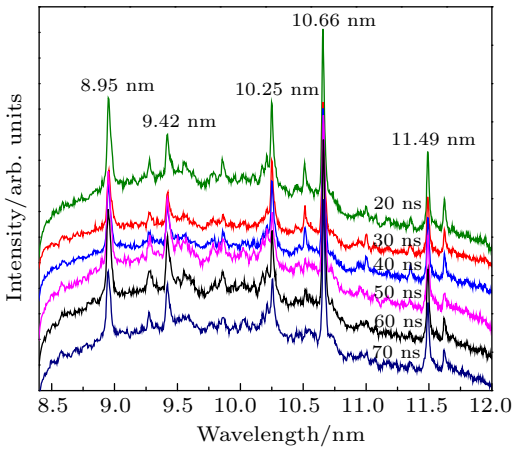


Fig. 2. Time evolution of extreme ultraviolet spectra of Cd produced by a laser power density of 2×10^{11} W/cm^2 at 0.5 mm from the target surface.

3. Atomic structure calculations and analysis

In earlier studies,[20] only 36 lines in the 8.0–11 nm range have been reported and identified as the 4p–5s resonance transitions of Cd^{11+}, Cd^{12+}, and Cd^{13+}; other lines between 11–12 nm are unknown. To determine new features and confirm prior identifications, calculations of the 4p–5s transitions from Cd^{9+} to Cd^{13+} were carried out by HFR using Cowan's codes.[18]

In these calculations, the electrostatic Slater–Condon F^k, G^k, and R^k integrals were reduced to 95%, the spin–orbit parameter ζ was retained, and the configuration interaction effects were considered. The calculations predicted that 4p–4d and 4d–4f configurations would enhance the 4p–5s transitions in Cd^{9+} to Cd^{11+}. The study also showed that important interactions affecting the $4s^24p^{k-1}5s$ configurations in Cd^{12+} and Cd^{13+} ions were $4s^24p^{k-1}nd$, $4s^14p^knf$, $4s^24p^{k-1}ms$, and $4s4p^k\varepsilon p$, in view of the important effects on the wavelengths and spectral line intensities. Note that $n = 4$–7, $m = 6$–7, and $\varepsilon = 5$–7 and k took the values of 6 (Cd^{12+}) and 5 (Cd^{13+}). To compare the spectra obtained from the experiment with theoretical output, the transition lines were calculated by convolving each line with a 0.05 eV full width at half maximum

(FWHM) Gaussian profile. It should be noted that the same parameters were assumed for each ion. The most intense peak in the 10.63–10.69 nm region was from a mixture of the Cd^{9+} and Cd^{10+} stages.

To evaluate the accuracy of the present calculations, a comparison between the results obtained in Ref. [20] and the present work is summarized in Tables 1–3. The similarity between a measured spectrum and calculated wavelengths helped the identification of the spectral lines. As can be seen in Tables 1 and 2, our calculations are consistent with calculations in Ref. [20]. The difference in the wavelengths had an error of approximately $\leqslant 0.04$ nm in most cases. Additionally, our calculation predicted new lines for Cd^{11+}, specifically,$^2D_{5/2}$–(^{3}P) $^2P_{3/2}$, $^2D_{3/2}$–(^{1}D) $^2D_{3/2}$, $^2D_{5/2}$–(^{3}D) $^2D_{3/2}$, and $^2D_{5/2}$–(^{1}P) $^2P_{3/2}$ transitions at 10.1 nm, 10.19 nm, 9.42 nm, and 8.51 nm, respectively. These lines showed a relatively high transition probability to the ground level, but had not been reported previously. Meanwhile, 20 levels were previously identified for Cd^{11+}. All levels of 4p–5s configurations in Cd^{11+} to Cd^{13+} reported in Ref. [20] were confirmed and some additional levels were established. The wavelengths were revised in this analysis and the values of the levels were also changed slightly. Furthermore, the ground configuration of Cd^{11+} was $4p^64d\ ^2D_{5/2,3/2}$ and the investigated $4p^54d5s$ configuration had 23 levels. The most excited states found were $4p^64d$–$4p^5nd$ ($n = 4$–6), $4p^64d$–$4p^54d\varepsilon s$ ($\varepsilon = 5$–7), and $4p^64d$–$4p^6mf$ ($m = 4$–6). Additionally, Cd^{12+} had six p-electrons forming a completely filled shell. Its excited state was obtained by excitation of one of the 4p electrons into $4p^5ns$ and $4p^5md$. The 4p–5s excitation gave only two levels. The ground state of Cd^{13+} was $4s^24p^5\ ^2P_{3/2,1/2}$ with $^2P_{3/2}$ lying deepest. The even excited states corresponded to $4p^4ns$ and $4p^4nd$ configurations. Eight levels were obtained in the 4p–5s transition.

Table 1. Comparison of the calculated wavelengths for resonance lines of the $4p^64d$–$4p^54d5s$ transition in Cd^{11+} ion.

Transition	Previous work(*)		This work		$\lvert\Delta\lambda\rvert$	$gA^{(b)}/10^{10}$ s^{-1}
	λ_{Exp}	λ^a_{Cal}	$\lambda_{Exp.}$	$\lambda_{Cal.}$		
$^2D_{3/2}$–(^{1}F) $^2F_{5/2}$	9.30	9.29	9.27	9.28	0.01	0.701
$^2D_{5/2}$–(^{1}F) $^2F_{5/2}$	9.39	9.38	9.37	9.36	0.02	20.224
$^2D_{5/2}$–(^{1}F) $^2F_{7/2}$	9.43	9.41	9.42	9.40	0.01	30.810
$^2D_{3/2}$–(^{1}D) $^2D_{5/2}$	9.51	9.49	9.42	9.47	0.02	30.205
$^2D_{5/2}$–(^{1}D) $^2D_{5/2}$	9.59	9.58	9.54	9.56	0.02	0.094
$^2D_{3/2}$–(^{3}D) $^2D_{5/2}$	9.77	9.73	9.79	9.71	0.02	0.228
$^2D_{5/2}$–(^{3}D) $^2D_{5/2}$	9.86	9.82	9.79	9.80	0.02	20.800
$^2D_{5/2}$–(^{3}D) $^4D_{7/2}$	9.91	9.88	9.86	9.85	0.03	9.058
$^2D_{3/2}$–(^{3}F) $^4F_{3/2}$	9.94	9.96	9.92	9.93	0.03	5.739
$^2D_{3/2}$–(^{3}F) $^2F_{5/2}$	9.95	9.92	9.86	9.89	0.03	30.098
$^2D_{3/2}$–(^{3}p) $^2P_{3/2}$	10.01	10.04	10.02	10.00	0.04	10.197
$^2D_{5/2}$–(^{3}F) $^4F_{3/2}$	10.04	10.05	10.02	10.02	0.03	7.472
$^2D_{5/2}$–(^{3}F) $^2F_{5/2}$	10.05	10.02	9.98	9.98	0.04	5.324
$^2D_{5/2}$–(^{3}F) $^2F_{7/2}$	10.09	10.08	10.03	10.04	0.04	5.621
$^2D_{3/2}$–(^{3}P) $^4P_{5/2}$	10.13	10.13	10.09	10.09	0.04	0.167
$^2D_{5/2}$–(^{3}F) $^4F_{5/2}$	10.14	10.14	10.11	10.10	0.04	0.945
$^2D_{3/2}$–(^{3}p) $^2P_{1/2}$	10.15	10.19	10.13	10.15	0.04	10.677
$^2D_{5/2}$–(^{3}F) $^4F_{7/2}$	10.18	10.19	10.13	10.14	0.05	4.120
$^2D_{5/2}$–(^{3}P) $^4P_{5/2}$	10.23	10.23	10.18	10.19	0.04	2.346

(*)Data from Ref. [20]. $\lambda_{Exp.}$ and $\lambda_{Cal.}$ denote experimental and calculated wavelengths and $|\Delta\lambda| = |\lambda^a_{Cal} - \lambda_{Cal}|$. (b)Present calculations.

Table 2. Comparison of the calculated wavelengths for resonance lines of the $4p^6$–$4p^55s$ and $4p^5$–$4p^45s$ transitions in Cd^{12+} and Cd^{13+} ions.

Ions	Transition	Previous work(*)		This work		$\lvert\Delta\lambda\rvert$	$gA^{(b)}/10^{10}$ s^{-1}
		$\lambda_{Exp.}$	$\lambda^a_{Cal.}$	$\lambda_{Exp.}$	$\lambda_{Cal.}$		
Cd^{12+}	$^1S^1_1P_1$	8.97	8.95	8.95	8.95	0.00	20.698
	$^1S^1_1P3$	9.45	9.44	9.42	9.42	0.02	20.320
Cd^{13+}	$^2P^2_{1/2}P_{1/2}$	9.00	9.00	8.95	9.00	0.00	20.287
	$^2P^4_{3/2}P_{5/2}$	9.05	9.04	9.05	9.03	0.01	8.082
	$^2P^4_{1/2}P_{1/2}$	9.28	9.26	9.24	9.25	0.01	0.0925
	$^2P_{3/2}$-$^4P_{3/2}$	8.95	8.96	8.95	8.95	0.01	20.433

(*)Data from Ref. [20]. λ_{Exp} and λ_{Cal} denote experimental and calculated wavelengths and $|\Delta\lambda| = |\lambda^a_{Cal} - \lambda_{Cal.}|$. (b)Present calculations.

Table 3. Comparison of the calculated energy levels of $4p^64d$, $4s^24p^6$, $4s^24p^5$, $4p^54d5s$, $4s^24p^55s$, and $4s^24p^45s$ arrays of Cd^{11+}, Cd^{12+}, and Cd^{13+} ions. The levels are designated in *LS* coupling scheme.

Ion	Config.	Designation	J	Previous work(*) E/cm^{-1}	This work E/cm^{-1}
Cd^{11+}	$4p^64d$	^{2}D	3/2	0	0
		^{2}D	5/2	9599	9214
	$4p^54d5s$	(^{3}P)^{2}P	1/2	985222	979948
		(^{3}P)^{4}P	5/2	987654	985257
		(^{3}F)^{4}F	7/2	992065	989363
		(^{3}F)^{4}F	5/2	996214	993308
		(^{3}P)^{2}p	3/2	998702	994266
		(^{3}F)^{2}F	7/2	1001001	999350
		(^{3}F)^{4}F	3/2	1005834	1002023
		(^{3}F)^{2}F	5/2	1005227	1005215
		(^{3}D)^{4}D	7/2	1018745	1018481
		(^{3}D)^{2}D	5/2	1023961	1024333
		(^{1}D)^{2}D	5/2	1052078	1050021
		(^{1}F)^{2}F	7/2	1069748	1068008
		(^{1}F)^{2}F	5/2	1074807	1071561
Cd^{12+}	$4s^24p^6$	^{1}S	0	0	0
	$4s^24p^55s$	(^{2}P)^{1}P	1	1058313	1061428
		(^{2}P)^{3}P	1	1115200	1117313
Cd^{13+}	$4s^24p^5$	^{2}P	3/2	0	0
		^{2}P	1/2	60636	59228
	$4s^24p^45s$	(^{3}P)^{4}P	5/2	1104932	1087171
		(^{3}P)^{4}P	3/2	1116526	1097227
		(^{3}P)^{4}P	1/2	1137786	1120018
		(^{3}P)^{2}P	3/2	1168603	1142720
		(^{3}P)^{2}P	1/2	1172136	1151173
		(^{1}D)^{2}D	5/2	1183852	1165486
		(^{1}D)^{2}D	3/2	1187930	1168012
		(^{1}S)^{2}S	1/2		1239189

(*)Data from Ref. [20].

Our results showed that the highest emission lines from gf-values belong to Cd^{10+} ions. Moreover, calculations of the emission line wavelengths for highly ionized Cd^{9+} to Cd^{10+} were in close agreement (the error was 0.01 nm or less) with experimental values. According to the J selection rules, the $4p^54d^35s$ and $4p^54d^25s$ excited configurations of Cd^{9+} and Cd^{10+} permitted 1860 lines in Cd^{9+}, extending from 8.78 nm to 12.60 nm; 371 transition lines to the ground level of Cd^{10+} were in the 8.62–11.47 nm region, but many were weak. Only transition lines with gf-values greater than 0.1 and agreement with the measured spectrum are listed in Tables 4 and 5.

Costello and O'Sullivan[20] observed spectra at 8–11 nm to study the 4p–5s resonance transition in Cd^{11+}, Cd^{12+}, and Cd^{13+}. In our new observation, the EUV spectrum was measured between 8.4–12 nm. Therefore, to predict theoretically longer wavelengths, we considered lower ionizations stages of Cd^{9+} and Cd^{10+}. The discrete line emissions of the 4p–5s resonance transition from the $4p^k4d^n$ ($k = 4$, 5 and $n = 0$–3) ground state presented in stages from Cd^{9+} to Cd^{13+}, and provided emission peaks characteristic for the structure.

To our knowledge, no measurements of level designations, wavelengths, oscillator strengths, and transition probabilities for 4p–5s of Cd^{9+} and Cd^{10+} were previously available, so our calculated results (Tables 4 and 5) are important for future assessment and comparisons.

Table 4. Measured and calculated wavelengths, weighted oscillator strengths (gf), and weighted transition probabilities (gA) for the strongest lines from the $4p^64d^3$–$4p^54d^35s$ transition in Cd^{9+} ion.

Transition		Wavelength/nm		gf(a)	$gA/10^{10}$ s^{-1}
$4p^64d^3\ ^4P_{5/2}$	$4p^54d^35s(^4p)^4D_{7/2}$	11.65	11.64	0.183	8.989
$4p^64d^3\ ^2D_{3/2}$	$4p^54d^35s(^2P)^2P_{3/2}$	11.49	11.49	0.143	7.219
$4p^64d^3\ ^2P_{3/2}$	$4p^54d^35s(^4F)^4G_{5/2}$	11.35	11.35	0.119	6.172
$4p^64d^3\ ^2D_{3/2}$	$4p^54d^35s(^2P)^4D_{5/2}$	11.30	11.29	0.185	9.704
$4p^64d^3\ ^2H_{9/2}$	$4p^54d^35s(^2H)^4I_{9/2}$	11.24	11.23	0.122	6.461
$4p^64d^3\ ^4F_{7/2}$	$4p^54d^35s(^4F)^4G_{9/2}$	11.18	11.18	0.191	10.02
$4p^64d^3\ ^4F_{3/2}$	$4p^54d^35s(^4F)^6G_{5/2}$	10.95	10.94	0.126	6.999
$4p^64d^3\ ^2G_{7/2}$	$4p^54d^35s(^2G)^2H_{9/2}$	10.66	10.66	0.577	30.39
$4p^64d^3\ ^2D_{3/2}$	$4p^54d^35s(^2D)^2D_{3/2}$	10.52	10.51	0.242	10.46
$4p^64d^3\ ^2G_{9/2}$	$4p^54d^35s(^2G)^2H_{11/2}$	10.45	10.46	0.349	20.13
$4p^64d^3\ ^2H_{11/2}$	$4p^54d^35s(^2H)^2H_{9/2}$	10.21	10.20	0.589	30.77
$4p^64d^3\ ^2G_{9/2}$	$4p^54d^35s(^2H)^2H_{9/2}$	10.10	10.11	0.208	10.36
$4p^64d^3\ ^4F_{9/2}$	$4p^54d^35s(^2H)^4H_{11/2}$	9.94	9.94	0.497	10.61
$4p^64d^3\ ^2F_{5/2}$	$4p^54d^35s(^4F)^4F_{3/2}$	9.86	9.88	0.154	10.05
$4p^64d^3\ ^2G_{7/2}$	$4p^54d^35s(^4P)^4P_{5/2}$	9.54	9.55	0.128	9.322
$4p^64d^3\ ^4F_{3/2}$	$4p^54d^35s(^4F)^4F_{3/2}$	9.50	9.50	0.128	9.469
$4p^64d^3\ ^4F_{7/2}$	$4p^54d^35s(^4F)^4F_{7/2}$	9.42	9.41	0.188	10.42
$4p^64d^3\ ^2H_{11/2}$	$4p^54d^35s(^2H)^2G_{9/2}$	9.27	9.27	0.215	10.67
$4p^64d^3\ ^4P_{5/2}$	$4p^54d^35s(^4P)^4S_{3/2}$	9.11	9.11	0.108	8.712

(a)Only transitions with $gf > 0.1$ are listed.

Table 5. Measured and calculated wavelengths, weighted oscillator strength (gf), and weighted transition probabilities (gA) for the strongest lines from the $4p^64d^2$–$4p^54d^25s$ transition in Cd^{10+} ion.

Transition		Wavelength/nm		gf[a]	$gA/10^{10}$ s^{-1}
Lower level	Upper level	$\lambda_{Exp.}$	$\lambda_{Cal.}$		
$4P^64d^2\ ^3F_3$	$4P^54d^25s(^3F)^3D_3$	10.73	10.73	0.141	8.158
$4P^64d^2\ ^1D_1$	$4P^54d^25s(^1D_1)^1D_1$	10.66	10.66	0.105	6.182
$4P^64d^2\ ^3F_3$	$4P^54d^25s(^1D)^3D_2$	10.60	10.60	0.145	8.615
$4P^64d^2\ ^1D_2$	$4P^54d^25s(^1D)^3F_3$	10.51	10.51	0.438	20.640
$4P^64d^2\ ^3F_2$	$4P^54d^25s(^3F)^5G_2$	10.21	10.20	0.179	10.150
$4P^64d^2\ ^3P$	$4P^54d^25s(^3P)^5D_1$	10.10	10.10	0.171	10.120
$4P^64d^2\ ^3F_4$	$4P^54d^25s(^3F)^3D_3$	10.03	10.03	0.376	20.490
$4P^64d^2\ ^1S$	$4P^54d^25s(^1S)^3P_1$	9.96	9.96	0.217	10.460
$4P^64d^2\ ^1G_4$	$4P^54d^25s(^1G)^3G_5$	9.93	9.93	0.543	30.670
$4P^64d^2\ ^3P_2$	$4P^54d^25s(^3P)^3S_1$	9.86	9.87	0.210	10.440
$4P^64d^2\ ^1G_4$	$4P^54d^25s(^3F)^3F_3$	9.54	9.55	0.144	10.050
$4P^64d^2\ ^3F_2$	$4P^54d^25s(3F)^3F_2$	9.27	9.27	0.170	10.320
$4P^64d^2\ ^3F_4$	$4P^54d^25s(^1G)^3F_4$	9.15	9.15	0.299	20.380
$4P^64d^2\ ^3P_1$	$4P^54d^25s(^3P)^3P_2$	8.94	8.94	0.108	9.027

[a]Only transitions with $gf > 0.1$ are listed.

Table 6. The predicted energy levels of $4p^64d^3$ and $4p^54d^35s$ arrays of Cd^{9+} ion. The levels are designated in *LS* coupling scheme.

Configuration	Designation	J	Energy/cm^{-1}
$4p^64d^3$	4F	3/2	0
	4F	7/2	7590
	4F	9/2	11517
	4P	3/2	21397
	2G	9/2	27393
	4P	5/2	27686
	2G	9/2	36278
	2H	11/2	36580
	2H	9/2	37763
	2P	3/2	43577
	2F	7/2	53242
	2F	5/2	53883
	2D	5/2	81282
	2D	3/2	82071
$4p^54d^35s$	$(^4P)^4D$	7/2	853398
	$(4F)^4G$	9/2	868566
	$(^2P)^2P$	3/2	869976
	$(^4F)^6G$	5/2	880546
	$(^2P)^4D$	5/2	885320
	$(^4F)^4G$	5/2	891866
	$(^2H)^4I$	9/2	894903
	$(^2G)^2H$	9/2	931666
	$(^2G)^2H$	11/2	950683
	$(^2H)^2H$	9/2	983391
	$(^2D)^2D$	3/2	1000195
	$(^2H)^4H$	11/2	1009069
	$(^4F)^4F$	3/2	1019436
	$(^4F)^4F$	3/2	1032026
	$(^4F)^4F$	7/2	1037463
	$(^4P)^4P$	5/2	1039841
	$(^2H)^2G$	9/2	1082706

Moreover, the ground levels of Cd^{9+} and Cd^{10+} possessed an open 4d, and the exciting configurations contained open ns, np, εf, and εd ($n = 5$–7, $\varepsilon = 4$–6) subshells; hence, there exist many hyperfine degenerate energy levels when they couple with the electrons of other shells. The ground configurations ($4p^64d^3$, $4p^64d^2$) of Cd^{9+} and Cd^{10+} had 19 and 9 levels, respectively, while the $4p^54d^35s$ and $4p^54d^25s$ configurations had 212 (Cd^{9+}) and 90 (Cd^{10+}) levels. The predicted energy levels resulting from the 4p–5s resonance transitions of Cd^{9+} and Cd^{10+} are listed in Tables 6 and 7. In these tables, the energy levels of the ground states ($4p^64d^3$, $4p^64d^2$) and excited states ($4p^54d^35s$, $4p^54d^25s$) of Cd^{9+} and Cd^{10+} were established. Figure 3 shows the calculated energy levels of the $4p^k4d^n$ ($k = 5$, 6 and $n = 0$–3) configurations and the spread of $4p^54d^n5s$ configurations in Cd^{9+} through Cd^{13+} below 160 eV.

Table 7. The predicted energy levels of $4p^64d^2$ and $4p^54d^25s$ arrays of Cd^{10+} ion. The levels are designated in *LS* coupling scheme.

Configuration	Designation	J	Energy/cm^{-1}
$4p^64d^2$	^3F	2	0
	^3F	3	6442
	^3F	4	12857
	^3P	0	22390
	^1D	2	22633
	^3P	1	25565
	^3P	2	32883
	^1G	4	34752
	^1S		75086
$4p^54d^25s$	$(^3F)^3D$	3	917770
	$(^1D)^3D$	2	928910
	$(^1D_1)^1D$	1	940360
	$(^1D)^3F$	3	953505
	$(^3F)^5G$	2	959456
	$(^3F)^3D$	3	989288
	$(^3P)^5D$	1	991554
	$(^1G)^3G$	5	1020888
	$(^1S)^3P$	1	1058752
	$(^3P)^3S$	1	1025485
	$(^3F)^3F$	2	1058534
	$(^3F)^3F$	3	1061255
	$(^1G)^3F$	4	1085129
	$(^3P)^3P$	2	1123405

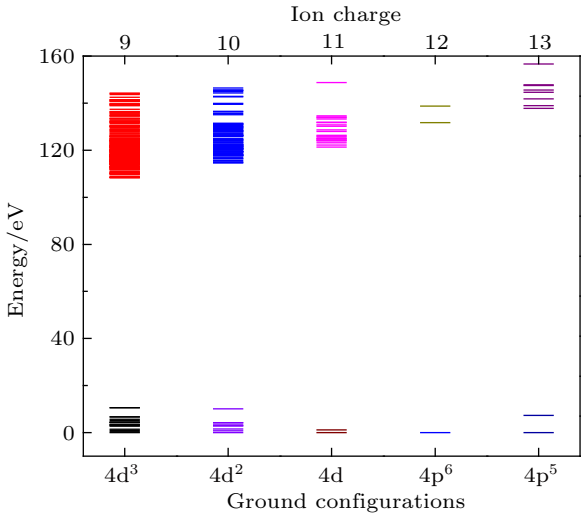


Fig. 3. Schematic overview of the calculated energy levels of the $4p^k4d^n$ ($k = 5$, 6 and $n = 0$–3) configurations in Cd^{9+} through Cd^{13+}. The vertical bars at the top show the spread of $4p^54d^n5s$ configurations below 160 eV.

4. Comparison between theoretical and experimental spectra

The variation in wavelengths as a function of charge state is the most important feature to compare with experimental data. The 4p–5s resonance transition arrays of mixtures of Cd^{9+} to Cd^{13+} result in emission peaks and are responsible for the structures. This characteristic feature was readily observed and identified in the measured spectra. The dominant contributions were from Cd^{9+} and Cd^{10+}.

To complete our simulations, the ion fractions of different stages as a function of electron density and electron temperature were calculated based on a steady-state CR model.[23] To the best of our knowledge, calculations of highly ionized Cd based on a CR model have not been studied previously. Figures 4(a) and 4(b) show the ion fractions of Cd^{9+} to Cd^{13+} as a function of electron temperature for an electron density $N_e = 5 \times 10^{20}$ cm^{-3} (Fig. 4(a)), and as a function of electron density for an electron temperature $T_e = 35$ eV (Fig. 4(b)). From these results, it is clear that T_e within 22–35 eV and N_e in the 1×10^{19} cm^{-3} to 5×10^{21} cm^{-3} range can be expected to produce Cd^{9+} to Cd^{13+} ions. For a number of lines (N) within 8.4–12 nm, an accurate identification would not be possible because only some data were sorted for comparison. The total synthetic emission profile was calculated by $I_{tot} = \sum_i g f_{i,k} F_i P_{i,k} \Gamma_{i,k}$, where $g f_{i,k}$ is the oscillator strength, F_i is the ion fraction, $P_{i,k} = \exp(-\Delta E/kT)$ is the Boltzmann factor, and $\Gamma_{i,k}$ is the associated Lorentzian profile function. For simplicity, we used the emission spectrum measured after 40 ns time delay as an example (Fig. 4). In Fig. 4, an experimental spectrum is compared with the simulation results obtained for an electron temperature of 34 eV and an electron density of 7×10^{20} cm^{-3}.

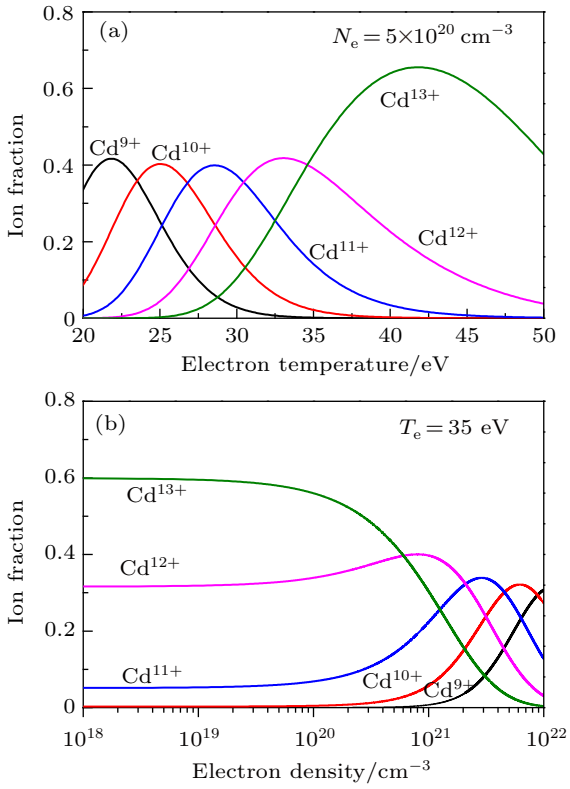


Fig. 4. Ion fractions for different ion stages as a function of (a) electron temperature and (b) electron density.

There was good agreement when the dominant fractional contribution rose with values of 6% (Cd^{9+}), 23% (Cd^{10+}), 40% (Cd^{11+}), 28% (Cd^{12+}), and 1% (Cd^{13+}) (see column chart insert in Fig. 5(a)). Figure 5(b) also presents the line profiles from Cd^{9+} to Cd^{13+} by assuming a normalized Boltzmann distribution among the excited states for the same conditions mentioned above. The same procedure was used to simulate the spectra after other time delays (Fig. 6). The comparison between the experimental and the simulated spectra yielded the relationships between the experimental conditions and plasma parameters. Figure 7 depicts the temporal evolution of the ion fractions of Cd^{9+} to Cd^{13+} at time delays ranging from 20 ns to 70 ns to gain a deeper understanding of the temporal characteristics of the ionized stages of highly charged ions from the Cd LPP spectra. The initial fraction at 20 ns was dominated by Cd^{11+} that gradually increased with increasing time delay (Fig. 7). However, with a time delay of 20 ns, the ion fractions of Cd^{12+} and Cd^{10+} were very close. For Cd^{12+}, the fractions increased until 30 ns and then decreased gradually, whereas Cd^{10+} showed the opposite pattern. It was noted that with an increasing time delay, Cd^{11+} and Cd^{10+} ions become more important after 30 ns. Moreover, the fractions of Cd^{9+} and Cd^{13+} ions were approximately constant along this sequence of time delays and had lower contributions.

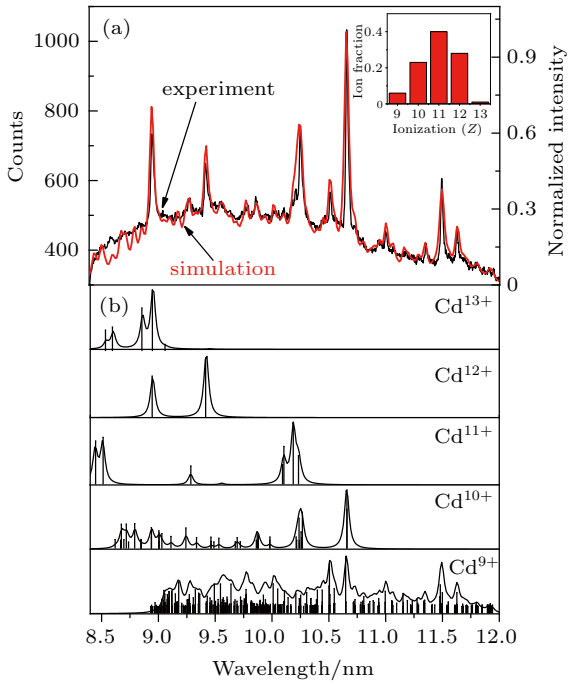


Fig. 5. Comparisons between the experiment (black line) recorded after 40 ns time delay and simulated spectra (red line). The column chart insert in (a) displays the ion fractions of Cd^{9+}, Cd^{10+}, Cd^{11+}, Cd^{12+}, and Cd^{13+}.

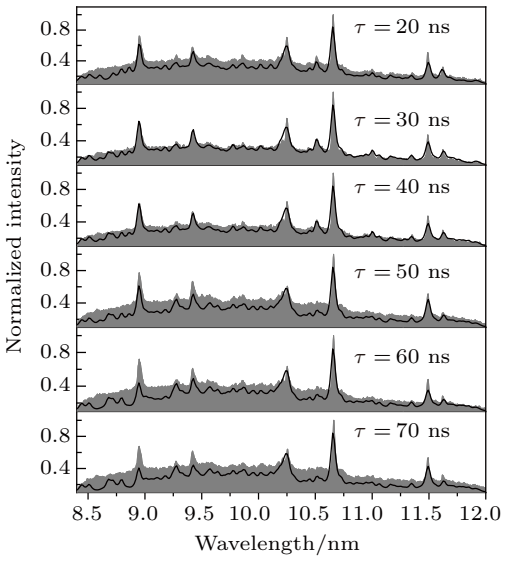


Fig. 6. Comparison between the measured (grey fill) and simulated (black lines) spectra after various time delays.

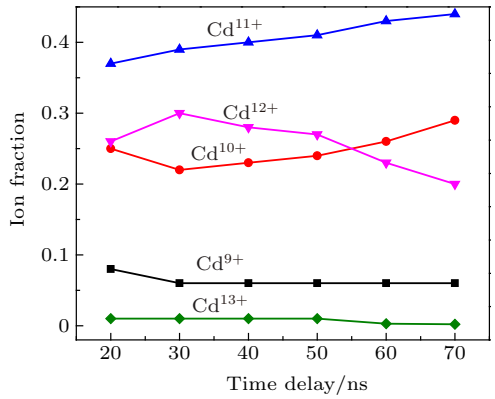


Fig. 7. Temporal behavior of the Cd^{9+} to Cd^{13+} ion fractions.

Figures 8 and 9 show the evolution of electron temperature and electron density with time delays from 20 ns to 70 ns, respectively. Their fitting relations are given in their respective graphs. The T_e is the electron temperature; N_e is the electron density; and t is the delay time. It was clear that the electron temperature displayed an exponential decay from 36 eV to 30 eV with increasing time delay. The electron density exhibited a sharp maximum at 20 ns and then a sharp decay to 30 ns with a more gradual decay thereafter. The decay of the electron temperature and electron density explains the free expansion behavior of LPPs in vacuum near the target surface.

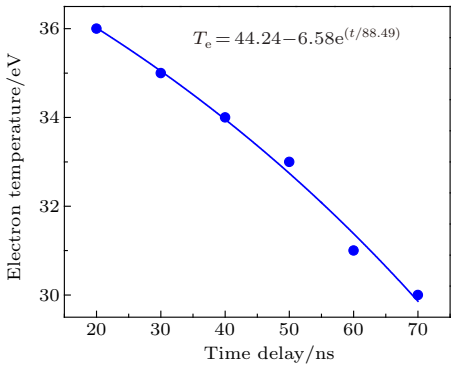


Fig. 8. Temporal behavior of electron temperature.

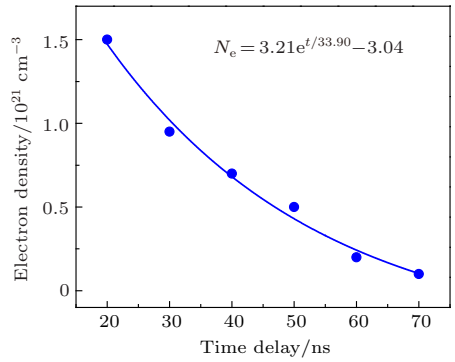


Fig. 9. Temporal behavior of electron density.

5. Conclusion and perspectives

The EUV emission spectra of Cd^{9+} to Cd^{13+} ions from laser-produced plasma were measured in the 8.4–12 nm region using a temporally and spatially resolved laser-produced plasma technique. The spectra dominated by a great number of lines from 4p–5s were analyzed using HFCI codes. A number of new features were identified for the first time and were tentatively assigned. Based on a steady-state CR model, plasma parameters were obtained for different ion stages by comparing experimental and simulated spectra. The simulated results for different time delays were in good agreement with the experimental spectra. In addition, the temporal evolution of electron temperature and electron density for Cd LPPs, and exponential decay of electron temperature and electron density were also described in this study. The results are helpful for astrophysics and plasma laboratory.

References

[1] Su M G, Min Q, Cao S Q, Sun D X, Hayden P, O'Sullivan G and Dong C Z 2017 *Sci. Rep.* **7** 1

[2] Su M G, Wang B, Min Q, Cao S Q, Sun D X and Dong C Z 2017 *Phys. Plasmas* **24** 013302

[3] Yoshikawa M, Pease R, Callen J, Witkowsi S and Velikhov E 1985 *Plasma Physics and Controlled Nuclear Fusion Research* (Vienna: IAEA). pp. 37–38

[4] Meyer-ter-Vehn J 2009 *Plasma Phys. Control. Fusion* **51** 124001

[5] Shigemori K, Kodama R, Farley D R, Koase T, Estabrook K G, Remington B A, Ryutov D, Ochi Y, Azechi H, Stone J and Turner N 2000 *Phys. Rev. E* **62** 8838

[6] Peacock N J and Pease R S 1969 *J. Phys. D: Appl. Phys.* **2** 1705

[7] Monchinsky V A, Kalagin I V and Govorov A I 1996 *Laser Part. Beams.* **14** 439

[8] Gwyn CW, Stulen R, Sweeney D and Attwood D 1998 *J. Vac. Sci. & Tech. B* **16** 3142

[9] Aota T and Tomie T 2005 *Phys. Rev. Lett.* **94** 015004

[10] Banine V Y, Koshelev K N and Swinkels G H 2011 *J. Phys. D: Appl. Phys.* **44** 253001

[11] Danylyuk S, Loosen P, Bergmann K, Kim H and Juschkin L 2013 *J. Micro/Nanolith. Mems Moems.* **12** 033002

[12] McCracken G M and Stott P E 1979 *Nucl. Fusion* **19** 889

[13] Even-Zohar M and Fraenkel B S 1972 *J. Phys. B: At. Mol. Phys.* **5** 1596

[14] Carroll P K, Costello J T and O'Sullivan G 1986 *Phys. Scr.* **33** 226

[15] O'Sullivan G, Costello J T and Carroll P K 1984 *J. Phys. B: At. Mol. Phys.* **17** 345

[16] Chaghtai M S, Rahimullah K and Khatoon S 1976 *Phys. Scr.* **14** 281

[17] Even-Zohar M, Fraenkel B S and Cowan R D 1974 *J. Phys. B: At. Mol. Phys.* **7** 5

[18] Cowan R D 1981 *The Theory of Atomic Structure and Spectra* (Berkeley: University of California Press) pp. 456–465

[19] Ryabtsev A N and Kononov E 2011 *Phys. Scr.* **84** 015301

[20] Costello J T and O'Sullivan G 1984 *J. Phys. B: At. Mol. Phys.* **17** 4477

[21] Charlotte Froese C 1978 *Compur. Phys. Commun.* **14** 145

[22] Grant I P, McKenzie B J, Norrington P H, Mayers D F and Pyper N C 1980 *Comput. Phys. Commun.* **21** 207

[23] Colombant D and Tonon G F 1973 *J. Appl. Phys.* **44** 3524

[24] Cao S Q, Su M G, Min Q, Sun D X, O'Sullivan G and Dong C Z 2018 *Phys. Plasmas.* **25** 023304